Dynamic Dual-Tracer PET Reconstruction

Fei Gao[1], Huafeng Liu[1], Yiqiang Jian[1], and Pengcheng Shi[2]

[1] State Key Laboratory of Modern Optical Instrumentation, Zhejiang University, HangZhou, Zhejiang, China
[2] Golisano College of Computing and Information Science, Rochester Institute of Technology, Rochester, NY, USA

Abstract. Although of important medical implications, simultaneous dual–tracer positron emission tomography reconstruction remains a challenging problem, primarily because the photon measurements from dual tracers are overlapped. In this paper, we propose a simultaneous dynamic dual–tracer reconstruction of tissue activity maps based on guidance from tracer kinetics. The dual–tracer reconstruction problem is formulated in a state–space representation, where parallel compartment models serve as continuous–time system equation describing the tracer kinetic processes of dual tracers, and the imaging data is expressed as discrete sampling of the system states in measurement equation. The image reconstruction problem has therefore become a state estimation problem in a continuous–discrete hybrid paradigm, and H_∞ filtering is adopted as the estimation strategy. As H_∞ filtering makes no assumptions on the system and measurement statistics, robust reconstruction results can be obtained for the dual-tracer PET imaging system where the statistical properties of measurement data and system uncertainty are not available *a priori*, even when there are disturbances in the kinetic parameters. Experimental results on digital phantoms, Monte Carlo simulations and physical phantoms have demonstrated the superior performance.

1 Introduction

Positron emission tomography (PET) is a functional molecular imaging technology which uses compounds labelled with positron emitting radioisotopes as molecular probes to image and measure biochemical processes of mammalian biology *in vivo*. Molecular probes for PET are developed by first identifying a target process to be studied and then synthesizing a positron labelled molecule, injected intravenously, through which an assay can be performed. With the increasingly wider availability of radiotracers, i.e. 18F–2-fluoro-2deoxy-D-glucose (FDG), 13N-ammonia, 11C–dihydrotetrabenazine(DTBZ) and 11C–WIN35,428, there have been many clinical and biomedical research applications in imaging various molecular *interactions* of biological processes.

Because of the complicated nature of the disease, the importance of multi–tracer PET imaging is well recognized yet seldom addressed because of paramount technical difficulties. Typically, multi–tracer imaging are treated as sequential problems, which are not well qualified for real time comparison in neuropharmcologic

J.L. Prince, D.L. Pham, and K.J. Myers (Eds.): IPMI 2009, LNCS 5636, pp. 38–49, 2009.

measurements and dynamic imaging between tracers. More crucially, the increased scanning time and suffering of patients hinder its practical applications. Hence, simultaneous multi–tracer imaging is of great recent interest.

Several attempts do try to tackle the dual-tracer imaging problem based on double–injection single–scan strategy[1,2,3,4,5]. However, all these works have been based upon the activity images are reconstructed as*a priori* using FBP or EM algorithm, and the aim is to use these maps to perform kinetic parameters estimation in some optimal sense. It is recognized that the recovery of activity maps of individual radio tracer is not a completely solved problem yet, and the great challenge here is that there is no direct way of separating signals from two different tracers as the modality based on measuring the 511 keV emitted by positron annihilations[1,2,6].

In this paper, we focus on simultaneous dynamic PET reconstruction of dual–tracer activity maps. The state–space representation is used to formulate the double–injection, single–scan protocol, where parallel compartment models for dual–tracer are coupled into state equations, while the mixed photon acquisition is integrated into measurement equations. The reconstruction problem therefore becomes a state estimation problem, and H_∞ filtering is applied to achieve robust estimation. Finally, respective dynamic reconstructed images for each tracer from digital Zubal phantom, Monte Carlo simulations and real phantom scan are presented as validations.

2 Methodology

2.1 Modeling of PET Measurement

In PET imaging, once radiopharmaceutical is injected or inhaled, it is transported and absorbed by the tissue of interests. An emitted positron meets a free electron and their annihilation produces two gamma ray photons traveling in opposite directions. If two photons are detected within the coincidence time window, an event is recorded along the line of response (LOR), and summing many of such events results in quantities that approximate line integrals (or equivalently projections and sinograms) through the radioisotope distribution.

Dynamic PET imaging involves a sequence of contiguous acquisition with different temporal resolutions, and a time series of activity images need to be reconstructed from the measurement data. The procedure can be formulated as a projection transform from image to data:

$$Y(t) = DX(t) + e(t) \tag{1}$$

$$X(t) = \Lambda\varphi(t) \tag{2}$$

here $Y(t)$ is the projection sinogram acquired from time frame 0 to time frame t, system probability matrix D is constructed from the physical and geometrical structure of PET acquisition system, $e(t)$ is the overall measurement errors in system, $\varphi(t)$ is a $n \times 1$ matrix representing the activity concentration in one

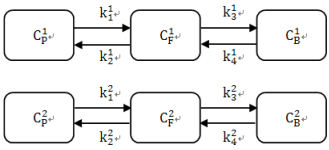

Fig. 1. Parallel dual–tracer two–tissue compartment model

tissue and Λ is a block $4n \times n$ diagonal matrix with blocks $[1 \quad 1 \quad 1 \quad 1]$ that help to extend to dual–tracer reconstruction simultaneously. To be in accordance with time configuration in dynamic PET imaging, The measurement equation is expressed as:

$$Y(t_k) = DX(t_k) + e(t_k) \tag{3}$$

here t_k ($k = 1, 2, \cdots, M$. M is the total number of the time frames) is the time point at the end of the kth time frame.

2.2 Modeling of Tracer Kinetics

Due to their simple implementation and biological plausibility, compartment models have been widely employed to quantitatively describe regional tracer kinetics in PET imaging. Model–driven tracer kinetics use a particular compartmental structure to describe the behavior of the tracer and allow for an estimation of either micro or macro system parameters [9]. The discrete nature of a compartment is what allow one to reduce the complex biological system into a finite number of discrete compartments and pathways [10].

In this paper, a parallel dual–tracer two–tissue compartment model is used to model the dual–tracer kinetic processes, with the structure shown in Fig. 1. The superscripts 1 and 2 correspond to parameters for the 1st tracer and the 2nd tracer respectively. C_P^1/C_P^2(pmol/ml) is arterial concentration of radiotracer 1/2. C_F^1/C_F^2(pmol/ml) is the concentration of non–specific binding tracer 1/2 in tissue. C_B^1/C_B^2(pmol/ml) is the concentration of specific binding tracer 1/2 in tissue. The parameters k_1^1/k_1^2, k_2^1/k_2^2, k_3^1/k_3^2 and k_4^1/k_4^2 are first-order rate constants specifying the tracer exchange rates between compartments for tracer 1/2. The two tissue compartment model satisfies many radioligand tracers well. Those include tracers such as 18F–FDG for the quantitative measurement of glucose metabolism, 11C–acetate for measurement of myocardial oxidative metabolism and monitor of tumor growth, and 62Cu–pyruvaldehyde bis[N4–methyl–thiosemicarbazone] (PTSM) for imaging blood flow. Note that two arterial input functions C_P^1 and C_P^2 are introduced into the tracers delivery process,

Table 1. Kinetic parameters for different tissue regions in Zubal thorax phantom

	k_1^{FDG}	k_2^{FDG}	k_3^{FDG}	k_4^{FDG}	$k_1^{acetate}$	$k_2^{acetate}$	$k_3^{acetate}$	$k_4^{acetate}$
ROI a	0.55951	2.75288	0.44793	0.01101	0.65188	0.22766	0.05311	0.03882
ROI b	0.37811	1.04746	0.13483	0.00857	0.45044	0.22871	0.07253	0.01417
ROI c	0.78364	1.15641	0.11200	0.02706	0.70372	0.53690	0.17755	0.01425

and each compartment model performs independently without interfering with the other. Using the model in Fig. 1, the time variation of kinetic model in an individual voxel can be denoted by the following first–order differential equations:

$$\frac{dC^1_{Fi}}{dt} = k^1_{1i}C^1_P(t) + k^1_{4i}C^1_{Bi}(t) - (k^1_{2i} + k^1_{3i})C^1_{Fi}(t) \tag{4}$$

$$\frac{dC^1_{Bi}}{dt} = k^1_{3i}C^1_{Fi}(t) - k^1_{4i}C^1_{Bi}(t) \tag{5}$$

$$\frac{dC^2_{Fi}}{dt} = k^2_{1i}C^2_P(t) + k^2_{4i}C^2_{Bi}(t) - (k^2_{2i} + k^2_{3i})C^2_{Fi}(t) \tag{6}$$

$$\frac{dC^1_{Bi}}{dt} = k^2_{3i}C^2_{Fi}(t) - k^2_{4i}C^2_{Bi}(t) \tag{7}$$

with subscript i representing a single voxel in reconstructed images. Equation(4)–Equation(7) can also be expressed in vector–space denotation as:

$$\begin{bmatrix} \dot{C}^1_{Fi}(t) \\ \dot{C}^1_{Bi}(t) \\ \dot{C}^2_{Fi}(t) \\ \dot{C}^2_{Bi}(t) \end{bmatrix} = \begin{bmatrix} -(k^1_{2i} + k^1_{3i}) & k^1_{4i} & 0 & 0 \\ k^1_{3i} & -k^1_{4i} & 0 & 0 \\ 0 & 0 & -(k^2_{2i} + k^2_{3i}) & k^2_{4i} \\ 0 & 0 & k^2_{3i} & -k^2_{4i} \end{bmatrix} \begin{bmatrix} C^1_{Fi}(t) \\ C^1_{Bi}(t) \\ C^2_{Fi}(t) \\ C^2_{Bi}(t) \end{bmatrix} + \begin{bmatrix} k^1_{1i} & 0 \\ 0 & 0 \\ 0 & k^2_{1i} \\ 0 & 0 \end{bmatrix} \begin{bmatrix} C^1_P(t) \\ C^2_P(t) \end{bmatrix} \tag{8}$$

The above equation can be expressed in a compact form as

$$\dot{x}_i(t) = a_i x_i(t) + b_i \tilde{C}_P(t) \tag{9}$$

where

$$x_i(t) = [\int_0^t C^1_{Fi}(\tau)d\tau, \int_0^t C^1_{Bi}(\tau)d\tau, \int_0^t C^2_{Fi}(\tau)d\tau, \int_0^t C^2_{Bi}(\tau)d\tau]$$

$$\tilde{C}_P(t) = [\int_0^t C^1_P(\tau)d\tau, \int_0^t C^2_P(\tau)d\tau]$$

$$a_i = \begin{bmatrix} -(k^1_{2i} + k^1_{3i}) & k^1_{4i} & 0 & 0 \\ k^1_{3i} & -k^1_{4i} & 0 & 0 \\ 0 & 0 & -(k^2_{2i} + k^2_{3i}) & k^2_{4i} \\ 0 & 0 & k^2_{3i} & -k^2_{4i} \end{bmatrix} \quad b_i = \begin{bmatrix} k^1_{1i} & 0 \\ 0 & 0 \\ 0 & k^2_{1i} \\ 0 & 0 \end{bmatrix}$$

The standard state transition equation for all the voxels can be constructed from Equation(9):

$$\dot{X}(t) = AX(t) + B\tilde{C}_P(t) + v(t) \tag{10}$$

where state vector $X(t) = [x_1(t)^T, x_2(t)^T, \cdots, x_n(t)^T]^T$ (n is the total number of voxels), A is a $4n \times 4n$ block diagonal matrix with block a_i, B is a $4n \times 2$ row block matrix with block b_i and $v(t)$ is a $4n \times 1$ vector describing model errors.

2.3 State Space Representation of PET Imaging

The state–space representation is introduced into the dynamic dual–tracer PET reconstruction problem, Equation(3) and Equation(10) form the state–space representation of dynamic dual–tracer PET reconstruction, in which parallel compartment models serve as a continuous time state equation to describe the tracer kinetic processes, and the projection data is expressed as discrete sampling of observation in a measurement equation. With given measurement $Y(t_k)$, the target of our dynamic dual–tracer reconstruction is to obtain the separate distribution of activity concentration for each tracer :

$$X_k^1 = \Lambda_1[X(t_{k+1}) - X(t_k)] \tag{11}$$

$$X_k^2 = \Lambda_2[X(t_{k+1}) - X(t_k)] \tag{12}$$

here Λ_1 and Λ_2 are $4n \times n$ block diagonal matrices with respective blocks $[1 \quad 1 \quad 0 \quad 0]$ and $[0 \quad 0 \quad 1 \quad 1]$. A robust H_∞ filtering algorithm described in the following section will be used for estimation in this state–space framework.

2.4 Robust Estimation of Dual Tracer Activity Maps

Since PET data after attenuation correction is not Poisson distributed, and have even more complicated statistics due to scatter events, scanner sensitivity and dead time correction. Instead of imposing certain distribution (Poisson or Shifted Poisson) on the data, the mini-max H_∞ estimation criterion is adopted in our filtering framework, which minimizes the worst possible effects of the disturbances on the state estimation errors, and requires no priori knowledge of noise statistics, making it an appropriate choice for PET reconstruction where the noise statistics is complicated. The H_∞ filtering strategy has been applied to static PET reconstruction [7] and dynamic single–tracer reconstruction [8] in previous efforts. Following this spirit, similar procedure is used in our work, while more sophisticated setting on parameters must be considered in dual–tracer situation. The state Equation(10) contains the separate components of each tracer, and thus the state noise and estimation error in respective kinetic process need to be estimated simultaneously during parallel calculation. Besides, the measurement equation(3) describes overlap sinogram data in dynamic time frames, so the mixed measurement noises should be incorporated into filtering strategy.

The objective function of H_∞ filtering is given by

$$\sup \frac{||X(t) - \tilde{X}(t)||^2_{Q(t)}}{||v(t)||^2_{V(t)^{-1}} + ||e(t)||^2_{W(t)^{-1}} + ||X_0 - \tilde{X}_0||^2_{H_0^{-1}}} \leqslant \gamma^2 \tag{13}$$

where $\tilde{X}(t)$ is the estimation of $X(t)$ at time t, the subscripts $Q(t)$, $V(t)^{-1}$, $W(t)^{-1}$ and H_0^{-1} denote the weighting matrices for the estimation error, the

state error, the measurement error and the initial value error, and γ^2 is a constant describing the disturbance level. Equation(13) defines the supremum of estimation error over all possible disturbances of noise energy. H_∞ criterion is a robust strategy to deal with the noise uncertainty in real situation. It is a game theory where the internal estimator plays against the external disturbances [11]. The complicated statistics of noises are not a required priori in this framework, and instead, we have only to maintain the small estimation errors with small disturbances, and vice versa. The minimum disturbance $\gamma^* \leq \gamma^2$ in equation(13) can also be expressed as a min-max problem:

$$\min_{X} \max_{V(t),W(t),X_0} \gamma^* = ||X(t)-\tilde{X}(t)||^2_{Q(t)} - \gamma^2(||v(t)||_{V(t)^{-1}} + ||e(t)||^2_{W(t)^{-1}} + ||X_0-\tilde{X}_0||^2_{H_0^{-1}}) \tag{14}$$

A complete solution to the H_∞ estimation problem for state–space model was present in [11], and the iterative equation is given as:

$$\tilde{X}(t_k) = A\tilde{X}(t_k^-) + H(t_k)[Y(t_k) - D\tilde{X}(t_k^-)] \tag{15}$$

$$H(t_k) = H(t_k^-)[I + C^T V(t)^{-1} C H(t_k^-)]^{-1} C^T V(t)^{-1} \tag{16}$$

where $H(t_k)$ is the filtering gain which satisfies the Riccati equation:

$$\dot{H}(t) = AH(t) + H(t)A^T + \frac{H(t)Q(t)H(t)}{\gamma^2} + N(t) \quad \text{with} \quad H(0) = H_0 \tag{17}$$

There are many numerical algorithms that solve this Riccati equation by successive integration. We adopt the scheme proposed in [12] to avoid the singularity during the process of iteration and obtain the stable solution.

3 Experiments

3.1 Experiments on Digital Phantoms

Simulation experiments are used to evaluate the accuracy and robustness of the simultaneous dual–tracer activity map reconstruction framework. Fig. 2 left shows a schematic representation of the Zubal thorax phantom, which has three distinctive tissue regions and a background region. The phantom is digitized at 32×32 pixels . Two regular tracers are used to simulate the injection and metabolic process: 18F-FDG for glucose metabolism and 11C-acetate for tumor growth monitor. The kinetic parameters of different regions are set from some known values in tracer kinetic research on FDG and acetate, as presented in Table 1. The plasma input function for 18F-FDG is simulated as:

$$C_P^{FDG}(t) = (A_1 t - A_2 - A_3)e^{-\lambda_1 t} + A_2 e^{-\lambda_2 t} + A_3 e^{-\lambda_3 t} \tag{18}$$

the parameters λ_i and A_i were selected for each tracer to match blood curves appearing in the literatures, here the value chosen were $A_1 = 851.1225 \mu Ci/mL/$

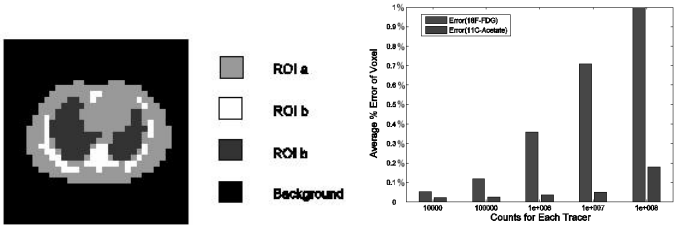

Fig. 2. Left: Zubal thorax phantom with multiple tissue regions indicated by different colors. Right: The APE of reconstructed images in the first group of experiments with different counting levels: 10^4, 10^5, 10^6, 10^7 and 10^8. For every pair, the left one is 18F, the right one is 11C.

min,$A_2 = 20.8113\mu Ci/mL$,$A_3 = 21.8798\mu Ci/mL$,$\lambda_1 = 4.133859min^{-1}$,$\lambda_2 = 0.01043449min^{-1}$ and $\lambda_3 = 0.1190996min^{-1}$. The plasma input function for 11C-acetate is obtained by correcting the whole-blood for circulating metabolites as [3]:

$$C_P^{acetate}(t) = [1 - 0.88(1 - e^{-(\frac{2\ln 2}{15}t)})]C_P^{FDG}(t) \tag{19}$$

With both input functions coupled into state equation(10), 18 frames of activity images were obtained from above compartment model simulations, sampled as $4 \times 0.5min$, $4 \times 2min$ and $10 \times 5min$. The system probability matrix in equation(1) was computed by using MATLAB toolbox developed by Prof. J.Fessler

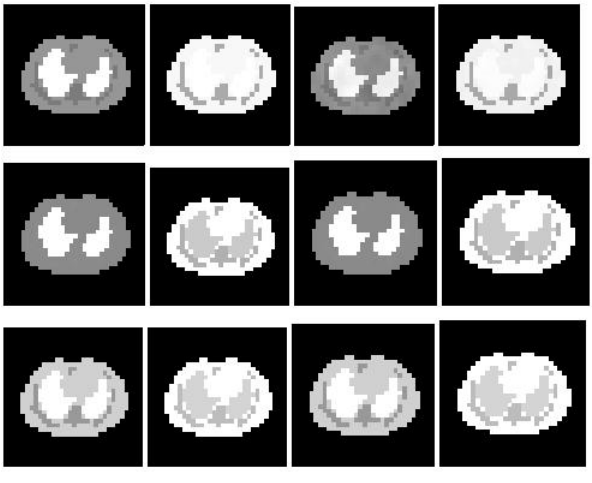

Fig. 3. The original and reconstructed activity images of 18F-FDG and 11C-acetate with perfect kinetic parameters and total 10^6 counts for time frame 2nd (top), 5th (middle) and 8th (bottom). 1st column: original 18F-FDG activity images; 2nd: original 18C-acetate activity images; 3rd: reconstructed 18F-FDG activity images; 4th: reconstructed 18C-acetate activity images.

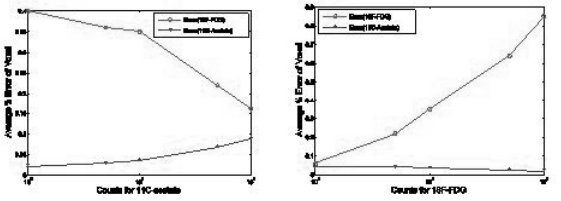

Fig. 4. The APE of reconstructed images with 18F and 11C of different count level. Left: the total counts of 18F-FDG were set to 10^6, and the counts of 11C-acetate varied from 10^5 to 10^7. Right: the total counts of 11C-acetate were set to 10^6, and the counts for 18F-FDG varied 10^5 to 10^7.

et al.. Then the activity images were projected into sinograms using a poisson model to generate raw data. Poisson-distributed random events were simulated and online subtracted. Two groups of simulation data were generated to evaluate the reconstruction performance. In every simulation, noise photons in simulated data was set to be about 30%. To analysis the reconstruction accuracy, we define a average percentage error(APE) for each tracer as:

$$APE = \frac{1}{N}\sum_i |\psi_{ik} - \tilde{\psi}_{ik}|/\psi_{ik} \tag{20}$$

here N is the total number of pixels, ψ_{ik} is the reconstructed activity values, $\tilde{\psi}_{ik}$ is the true values. In the first group of simulation data, We generated sinograms with the count levels of 18F and 11C being similar. 5 different count levels: 10^4, 10^5, 10^6, 10^7 and 10^8 were used in the data generation, which represent the total counts of the simulated data. The purpose here is to see the different reconstruction results at different count levels. Fig. 2 right presents the APE of reconstructed results in these five groups of experiments, the APE of reconstructed images for each pair of tracers increased with the overall counts increasing. The comparison between the original images and reconstructed images of count level 10^6 is shown in Fig. 3, where the APE for simulated 18F-FDG reconstruction is 0.360%, and the APE for simulated 11C-acetate reconstruction is 0.037%. The second group of simulations was performed with 18F and 11C of different count level. The purpose here is to see the interaction between the

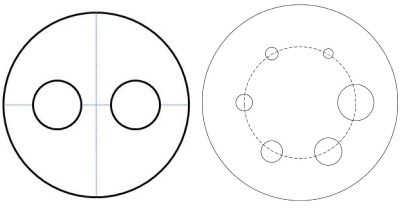

Fig. 5. The transverse view of phantoms. Left: the phantom used for Monte Carlo simulation; Right: the 6-sphere phantom used for real PET scan.

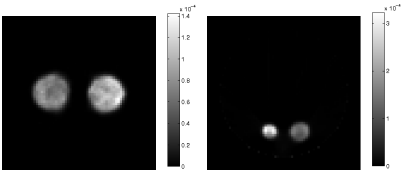

Fig. 6. The EM reconstruction of simulation data and real phantom scan data. Left: Monte Carlo simulation data; Right: real phantom scan data.

two tracers. As shown in Fig. 4 left, the total counts of 18F-FDG were set to 10^6, and the counts for 11C-acetate varied from 10^5 to 10^7 with an interval of 5×10^5. The APE of 11C-acetate reconstructed images increased from 0.022% to 0.085%, and the APE of 18F-FDG images decreased from 0.400% to 0.161%. Fig. 4 right gives an analogous result by setting the total counts of 11C-acetate as 10^6 and that for 18F-FDG varied from 10^5 to 10^7. In this experiment, the APE for 18F-FDG images increased from 0.075% to 0.850%, and the APE for 11C-acetate images decreased from 0.045% to 0.021%.

3.2 Experiments with Data from Monte Carlo Simulations

The second data set used for validation in this study was acquired by Monte Carlo simulations [13]. The simulated scanner is Concord microPET R4, and a 6cm diameter cylindrical phantom with 2 hot regions was used. The transverse view of the phantom is shown in Fig. 5 left, the phantom was filled with pure water, two hot regions were filled with 18F–FDG solutions and 11C–acetate solutions respectively, the initial activity concentration was set to 2.315kBq/ml. A simulation of a dynamic sequence of 10 frames over 160 minutes(10×16min) from the mixed effect of dual tracers was performed, the final generated sinogram data set has 128×128 projections for every slice. First several static reconstruction were performed, then the kinetic parameters k_1^1/k_1^2, k_2^1/k_2^2, k_3^1/k_3^2 and k_4^1/k_4^2 in the parallel compartment models used here were calculated using these static reconstruction results by COMKAT [14]. Since this is a Monte Carlo simulation, we can get the true activity concentration at every time frame. The reconstructed images at time frame 1 by traditional EM algorithm is shown in Fig. 6 left, the activity concentrations of 18F and 11C can not be separated. The respective images of 18F–FDG and 11C–acetate were reconstructed by our framework simultaneously, Fig. 7 shows the true images and the reconstructed images at time frame 1, 2, 5 and 8.

Table 2. Statistical studies of estimated 18F activity distribution

	Frame1	Frame2	Frame5	Frame8
bias	-0.0343	-0.0313	-0.0812	0.2432
std	0.2378	0.3664	0.2878	0.4461

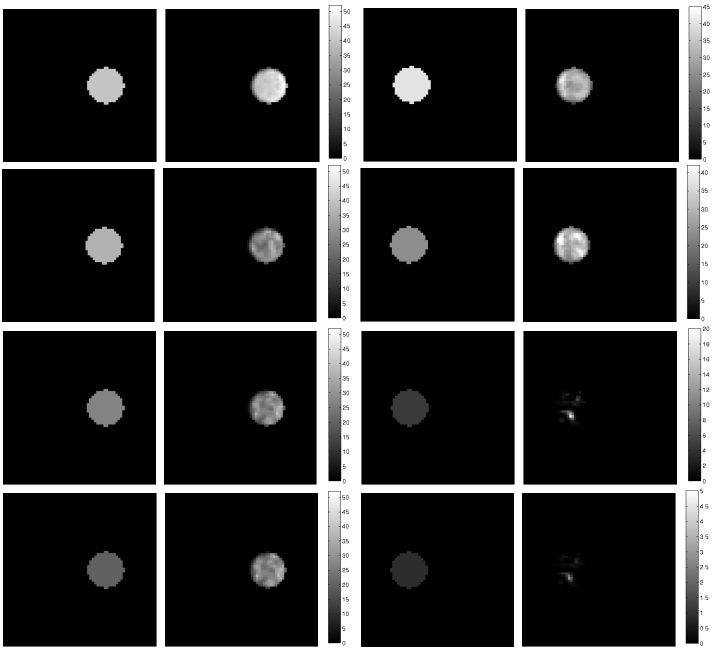

Fig. 7. The true and reconstructed activity images of 18F-FDG and 11C-acetate with data set from Monte Carlo simulations, from top to bottom, 4 rows correspond to the 1st, 2nd, 5th and 8th time frame. The 1st column is the true 18F-FDG activity images; the 2nd column is reconstructed 18F-FDG activity images; the 3rd column is the true 11C-acetate activity images; the 4th column is reconstructed 11C-acetate activity images.

A statistical analysis on reconstructed images against true values in the hot regions is performed. Let N_p be the total number of pixels and XR_i be the final reconstruction result of pixel i respectively, and XT_i be true value of corresponding pixel i, then we have the following error definitions:

$$bias = (1/N_p) \sum_i (XR_i - XT_i)/XT_i \tag{21}$$

$$std = (1/(N_p - 1)) \sum_i^i ((XR_i - XT_i)/XT_i)^2)^{0.5} \tag{22}$$

The calculated bias and standard derivation values of the reconstruction images from different time frames are summarized in Table 2 and Table 3, Table 2 is bias and standard derivation values for 18F–FDG reconstruction and Table 3

Table 3. Statistical studies of estimated 11C activity distribution

	Frame1	Frame2	Frame5	Frame8
bias	-0.2983	0.1979	-0.7256	-0.7894
std	0.3445	0.4016	0.9053	0.8930

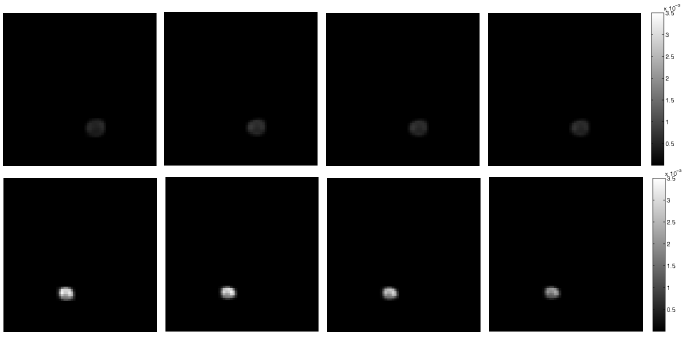

Fig. 8. The reconstructed activity images of 18F-FDG and 11C-acetate with data set from real phantom scan. The 1st row is the reconstructed 18F-FDG images, the 2nd row is the reconstructed 11C-acetate images. From left to right, 4 columns correspond to time frame 1, 2, 5 and 8 respectively.

is bias and standard derivation values for 11C–acetate reconstruction. Since the half–life of 18F–FDG is 110 minutes and that of 11C-acetate is only about 20 minutes, 11C–acetate decayed faster than 18F–FDG, so the standard derivation values of 18F–FDG first decrease at frame 5 due to the faster decay of 11C–acetate, and then increase at frame 8 due to its self-decay, the standard derivation values of 11C-acetate increase continuously though all former frames due to its fast decay, after frame 5, the standard derivation values keep high because the low concentration of 11C–acetate in the phantom.

3.3 Experiments with Physical Phantom Scanning Data

The real data set used in this study was acquired on the Hamamatsu SHR-22000 scanner using a 6 – spheres phantom, which is usually used to measure the recovery coefficient. The SHR-22000 is designed as a whole body imaging system. It has a 838mm detector ring diameter with a patient aperture of 600mm, an axial field of view (FOV) of 224mm, can operate in 2D or 3D mode. For the phantom, there are six circular regions of different diameters. These sphere objects have diameters of 37mm, 28mm, 22mm, 17mm, 13mm, 10mm and are inserted in a circular cylinder with diameter of 200mm corresponding to a volume of 9300ml, as shown in Fig. 5 right. The phantom filled with pure water was located at the center of both transaxial and axial FOV in the scanner using the patient bed. We injected 22mCi 11C–acetate solution into the 28mm diameter sphere and 5 minutes later injected 8mCi 18F–FDG solution into the 37mm diameter sphere. Acquirement of a dynamic sequence of 10 frames over 20 minutes(10×2min) from the mixed effect of dual tracers was performed, the final generated sinogram data has 192×192 projections for every slice. The kinetic parameters used were also calculated by COMKAT like above section. The reconstructed image at time frame 1 by EM algorithm is shown in Fig. 6 right for comparison. The respective images of 18F–FDG and 11C–acetate were reconstructed by our

framework simultaneously, Fig. 8 shows the reconstructed images at frame 1, 2, 5 and 8. The two tracers are correctly reconstructed respectively, it is evident that this framework is effective for double–injection single–scan PET reconstruction of dual–tracer activity maps.

Acknowledgements

This work is supported in part by the National Natural Science Foundation of China(No: 60772125), and by a Development Project of Zhejiang Province (NO: 2008C23060).

References

1. Huang, S.C., Carson, R.E., Hoffman, E.J.: An investigation of a double-tracer technique for positron computerized tomography. Journal of Nuclear Medicine 23, 816–822 (1982)
2. Koeppe, R.A., Raffel, D.M., Snyder, S.E.: Dual-[11C] Tracer Single-Acquisition Positron Emission Tomography Studies. Journal of Cerebral Blood Flow & Metabolism 21, 1480–1492 (2001)
3. Kadrmas, D.J., Rust, T.C.: Feasibility of rapid multi-tracer PET tumor imaging. Nuclear Science Symposium Conference Record 4, 2664–2668 (2004)
4. Rust, T.C., Dibella, E.V., McGann, C.J.: Rapid dual-injection single-scan (13) N-ammonia PET for quantification of rest and stress myocardial blood flow. Physics in Medicine and Biology 51, 5347–5362 (2006)
5. Hayashi, T., Kudomi, N., Watabe, H.: A rapid CBF/CMRO2 measurement with a single PET scan with dual-tracer/integration technique in human. Journal of Cerebral Blood Flow & Metabolism 25, S609 (2005)
6. Black, N.F., McJames, S., Rust, T.C.: Evaluation of rapid dual-tracer 62Cu-PTSM + 62Cu-ATSM PET in dogs with spontaneously occurring tumors. Physics in Medicine and Biology 53, 217–232 (2008)
7. Liu, H., Tian, Y., Shi, P.: PET image reconstruction: A robust state space approach. In: Christensen, G.E., Sonka, M. (eds.) IPMI 2005. LNCS, vol. 3565, pp. 197–209. Springer, Heidelberg (2005)
8. Tong, S., Shi, P.: Tracer kinetics guided dynamic PET reconstruction. In: Karssemeijer, N., Lelieveldt, B. (eds.) IPMI 2007. LNCS, vol. 4584, pp. 421–433. Springer, Heidelberg (2007)
9. Gunn, R.N., Gunn, S.R., Turkheimer, F.E.: Positron Emission Tomography Compartmental Models: A Basis Pursuit Strategy for Kinetic Modeling. Journal of Cerebral Blood Flow & Metabolism 21, 635–652 (2001)
10. Cobelli, C., Foster, D., Toffolo, G.: Tracer Kinetics in Biomedical Research: From Data to Model. Kluwer Academic/Plenum Publishers, New York (2000)
11. Shen, X., Deng, L.: A dynamic system approach to speech enhancement using the H1 filtering algorithm. IEEE Transactions on Speech and Audio Processing 7(4), 391–399 (1997)
12. Schiff, J., Shnider, S.: A natural approach to the numerical integration of Riccati differential equations. SIAM Journal on Numerical Analysis 36, 1392–1413 (1996)
13. Jan, S.: GATE: a simulation toolkit for PET and SPECT. Physics in Medicine and Biology 49, 4543–4561 (2004)
14. Muzic, R.F., Cornelius, S.: COMKAT: Compartment Model Kinetic Analysis Tool. Journal of Nuclear Medcine 42, 636–645 (2001)